University of Texas Rio Grande Valley

ScholarWorks @ UTRGV

Mechanical Engineering Faculty Publications and Presentations

College of Engineering and Computer Science

2-18-2020

On the spreading of non-canonical thermals from direct numerical simulations

Kai Liu

Nadim Zgheib

S. Balachandar

Follow this and additional works at: https://scholarworks.utrgv.edu/me_fac

 Part of the Mechanical Engineering Commons

Physics of Fluids

On the spreading of non-canonical thermals from direct numerical simulations

Cite as: Phys. Fluids **32**, 026602 (2020); https://doi.org/10.1063/1.5138981
Submitted: 18 November 2019 • Accepted: 29 January 2020 • Published Online: 18 February 2020

Kai Liu, N. Zgheib and S. Balachandar

View Online Export Citation CrossMark

ARTICLES YOU MAY BE INTERESTED IN

Deep learning methods for super-resolution reconstruction of turbulent flows
Physics of Fluids **32**, 025105 (2020); https://doi.org/10.1063/1.5140772

Tip vortices formation and evolution of rotating wings at low Reynolds numbers
Physics of Fluids **32**, 021905 (2020); https://doi.org/10.1063/1.5134689

Dynamics of a circular cylinder with an attached splitter plate in laminar flow: A transition from vortex-induced vibration to galloping
Physics of Fluids **32**, 027104 (2020); https://doi.org/10.1063/1.5125588

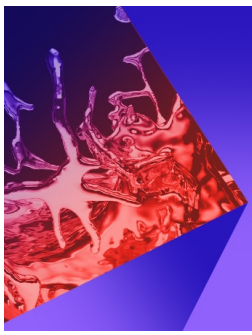

Physics of Fluids
Special Topic: Paint and Coating Physics
Submit Today!

AIP Publishing

© 2020 Author(s).

Physics of Fluids ARTICLE scitation.org/journal/phf

On the spreading of non-canonical thermals from direct numerical simulations

Cite as: Phys. Fluids 32, 026602 (2020); doi: 10.1063/1.5138981
Submitted: 18 November 2019 • Accepted: 29 January 2020 •
Published Online: 18 February 2020

View Online Export Citation CrossMark

Kai Liu,[1] N. Zgheib,[1,2,a)] and S. Balachandar[1]

AFFILIATIONS

[1] Department of Mechanical and Aerospace Engineering, University of Florida, Gainesville, Florida 32611, USA
[2] School of Engineering, Lebanese American University, Byblos 1401, Lebanon

[a)] **Author to whom correspondence should be addressed:** nadim.zgheib@lau.edu.lb

ABSTRACT

We present results from direct numerical simulations on laminar and turbulent non-canonical thermals with an initial rectangular density distribution at a Reynolds number of $Re = 500$ and $Re = 5000$, respectively. We find the non-canonical shape to induce strong azimuthal variations in the thermal for both the laminar and turbulent cases. These include noticeable differences in downward and horizontal propagation speeds as well as differences in the strength of the vortex tube. These differences persist over a significant period of time and help generate a cross-flow component that is otherwise not present in canonical cases. The cross-flow component is in the opposite direction to that observed in gravity currents with the same initial density distribution. This is counterintuitive seeing that both flows are solely driven by buoyancy. By extracting the three-dimensional streamlines, we find the descending vortex tube to force the dense fluid to follow a helical path.

Published under license by AIP Publishing. https://doi.org/10.1063/1.5138981

I. INTRODUCTION

Thermals are a class of buoyancy driven flows (Turner, 1963; 1964; Richards, 1961; Zhao *et al.*, 2013; Lecoanet and Jeevanjee, 2018; Gao and Yu, 2016; and Hasnain and Alba, 2017). A typical example is a hot packet of air rising through its surroundings. The hot air packet is less dense than the surrounding cooler air and is, thus, driven upward by buoyancy. Alternatively, a cooler packet of air descending in a warmer environment is also termed a thermal, usually with the specification that the thermal is negatively buoyant to indicate downward or sinking motion. In these two examples, the thermal is composed of the same material as its surroundings, and the density difference, and consequently the driving mechanism behind the flow, is a result of a temperature variation. While the name "thermal" is indicative of a temperature related phenomenon, the density difference may arise from other factors such as salinity, concentration, or different fluids altogether. The flow does not require large density variations; in fact, a relative density difference of less than a percent is sufficient to generate a thermal. Thermals encompass a variety of environmental and industrial flows and are thus of interest to the scientific and engineering communities. A typical example includes the flow resulting from a dredging process in which relatively dense solution is suddenly released into the relatively less dense sea water. It should be noted here that the thermal propagation should be predominantly along the vertical direction, that is, it should be mostly aligned with the gravitational field. In the limit where a strong component of the flow is horizontal, the flow is usually termed a gravity current (e.g., Huppert and Simpson, 1980 and Ottolenghi *et al.*, 2016).

Thermals have been predominantly studied in one of two canonical cases. The term canonical here is solely in reference to the initial shape of the buoyant fluid. When the initial shape is axially symmetric such as in the case of a circular cylinder (e.g., Bond and Johari, 2005) or when the initial shape is a rectangular parallelepiped with one side having the same extent as that of the ambient fluid (e.g., Turner, 1969), the thermal is termed a canonical thermal. While the initial buoyancy source can be of any shape, studies pertaining to non-canonical thermals, i.e., thermals where the initial buoyant source does not conform to the above two cases have remained limited.

For instance, Bond and Johari (2005) examined axially symmetric thermals with various initial height-to-diameter aspect ratios. They found that the flow may be divided into two main phases: an initial acceleration phase, where the thermal accelerated from rest to reach its maximum velocity, and a subsequent phase, where the flow decelerates and displays thermal-like characteristics. They observed

the flow characteristics in the first phase to be dependent on the initial geometry, while those in the second phase to be independent of initial geometry, albeit for axially symmetric thermals.

A possible reason for the scarcity of studies of non-canonical thermals is the underlying assumption that they would largely resemble the canonical axially symmetric case. Recent experiments of particle-laden thermals (Wei Er *et al.*, 2016) have shown, however, that initially rectangular buoyant sources can exhibit qualitative differences compared to their axially symmetric counterparts. Such differences include azimuthal variations in descent speeds as well as longitudinal and transverse spreading rates that may persist well after the initial release. A thorough examination of the physics responsible for such differences is still missing.

The purpose of this study is to use direct numerical simulations to study canonical and non-canonical rectangular thermals in the laminar and turbulent regimes. The main objective is to understand and highlight the differences associated with non-canonical thermals and use the resolved flow and concentration fields to extract the underlying mechanisms behind the observed differences.

This paper is structured as follows. In Sec. II, we provide a description of the mathematical model and discuss the influence of boundary conditions. In Sec. III, we showcase the simulation results and highlight the peculiarities in flow structure pertaining to non-canonical thermals. In Sec. IV, we discuss possible explanations for the aforementioned peculiarities. Finally, concluding remarks are given in Sec. V.

II. MATHEMATICAL SETUP AND INITIAL CONDITION

In this section, we will briefly go over the numerical setup and governing equations in Sec. II A and discuss the effects of the upper boundary on the short- and long-term evolution of the thermal in Sec. II B.

A. Governing equations

The simulations are carried out inside a rectangular box and consist of instantaneously releasing a finite volume of negatively buoyant (denser) fluid into a still environment, as shown in Fig. 1. The fluids are miscible, and aside from the density difference, they are chosen to have the same properties. The non-dimensional governing equations consist of conservation of mass (1) and momentum (2), and a transport equation (3) for the density field,

$$\nabla \cdot \boldsymbol{u} = 0, \tag{1}$$

$$\frac{D\boldsymbol{u}}{Dt} = \rho \boldsymbol{e}^g - \nabla p + \frac{1}{Re}\nabla^2 \boldsymbol{u}, \tag{2}$$

$$\frac{\partial \rho}{\partial t} + \nabla \cdot (\rho \boldsymbol{u}) = \frac{1}{ScRe}\nabla^2 \rho. \tag{3}$$

In Eqs. (1)–(3), $\boldsymbol{u}$, ρ, and p denote the three-dimensional velocity vector, density, and pressure fields, respectively. Density is normalized to values between 0 and 1. The lower limit ($\rho = 0$) corresponds to ambient fluid, and the upper limit ($\rho = 1$) corresponds to the density of the heavier fluid, i.e., the thermal, at the time of release ($t = 0$). Any in-between value of the density ($0 < \rho < 1$) at later times

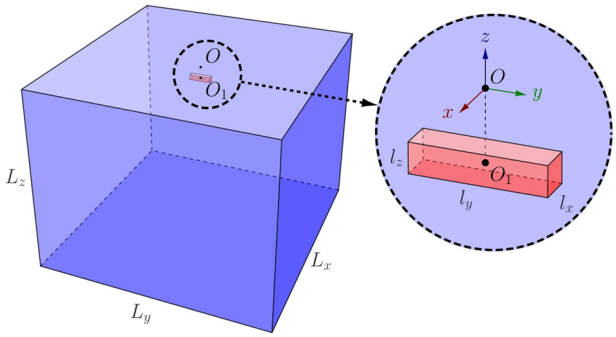

FIG. 1. Schematic of the rectangular numerical domain with an enlarged view of the initial non-canonical dense fluid distribution. The numerical domain, highlighted in blue, has dimensions $L_x \times L_y \times L_z$ and is initially filled with light ambient fluid (ρ_a^*). A small portion of the domain, highlighted in red, of dimensions $l_x \times l_y \times l_z$ represents the dense fluid (ρ_{c0}^*) distribution at time of release $t = 0$. The Cartesian coordinate system is anchored at the center of the top boundary. O_1 is the geometric center of the dense fluid.

is a result of mixing between the two fluids. The density field is, thus, defined as

$$\rho = \frac{\rho^* - \rho_a^*}{\rho_{c0}^* - \rho_a^*}. \tag{4}$$

Here, ρ^*, ρ_a^*, and ρ_{c0}^* represent the local, ambient, and initial heavy fluid densities, respectively. Throughout the manuscript, the asterisk will refer to dimensional quantities, and all other quantities are to be understood as non-dimensional. We assume the density difference between both fluids to be small, which justifies the use of the Boussinesq approximation where density variations are neglected except for the gravity term, the first term on the right-hand side of (2). In fact, the present situation in which the dense and ambient fluids differ only by their densities may be representative of the case where the ambient fluid corresponds to tap water and the dense fluid corresponds to tap water with a small concentration of salt (e.g., Sànchez *et al.*, 1989). Another example of relevance to dredging is when the excess density is due to a dilute distribution of fine sediment. The excess density due to salt or sediment would typically be around one tenth of a percent which justifies assuming both fluids to have similar thermo-physical properties except for their densities. Furthermore, the pressure is rendered non-dimensional using a dynamic pressure scale,

$$p = \frac{p^*}{\rho_a^* U^{*2}}, \tag{5}$$

with p^* being the local dimensional pressure and U^* denoting the velocity scale to be defined shortly. The $\boldsymbol{e}^g$ term in the right-hand side of the momentum equation is a unit vector pointing in the direction of gravity (i.e., downward). The two non-dimensional parameters that result from the non-dimensionalization of the above system are the Schmidt and Reynolds numbers defined as

$$Sc = \frac{\nu^*}{\kappa^*}, \quad Re = \frac{\Lambda^* U^*}{\nu^*}, \tag{6}$$

Published under license by AIP Publishing

where ν^* and κ^* are the kinematic viscosity and molecular diffusivity of the ambient fluid, respectively. In the expression for *Re*, length and velocity scales are defined as

$$\Lambda^* = (V_0^*)^{1/3}, \quad U^* = \sqrt{g^* \frac{\rho_{c0}^* - \rho_a^*}{\rho_a^*} \Lambda^*}, \tag{7}$$

where V_0^* is the initial volume of heavy fluid and g^* is the local gravitational acceleration. Consequently, the time scale is straightforwardly obtained as the ratio of the above two scales,

$$T^* = \frac{\Lambda^*}{U^*}. \tag{8}$$

While *Re* provides a measure of flow strength and turbulence, the Schmidt number provides a measure of the diffusivity of the thermal-ambient interface. Turbulent flows with $Sc \ll 1$ tend to have a relatively diffuse interface, where the density variation across the interface is gradual. In contrast, weakly turbulent flows with $Sc \gg 1$ usually exhibit sharp variations in density between the ambient and the thermal, often resulting in a sharp density jump at the interface. On the other hand, the effects of the Schmidt number on the thickness of the interface become marginal for turbulent flows. In such flows, the mixing is dominated by Kelvin–Helmholtz vortices and smaller scale instabilities rather than by molecular diffusivity of the fluids (e.g., Bonometti and Balachandar, 2008).

The governing equations are solved using the parallel, spectral element code, Nek5000 (Fischer *et al.*, 2008). The numerical domain is divided into multiple rectangular elements, and each element contains a fixed number of grid points along each of the three directions. The number of grid points within each element depends on the polynomial order used. For example, an eighth order polynomial along the *x*-direction implies that there are nine grid points (the last point is actually the first point of the next neighboring element) within each element along the *x*-direction. In all our simulations, the polynomial order, and thus, the number of grid points, is taken to be the same along each of the three directions. Therefore, the total number of grid points, along, say, the *x*-axis, is nothing but the product of the number of elements by the polynomial order in the *x*-direction. To obtain spectral accuracy, the points within each element are not distributed uniformly but rather as Gauss–Lobatto–Legendre points.

A total of 11 simulations were conducted, the details of which are listed in Table I. Each simulation required 4 h of computation time on 128 cores for the laminar cases and 30 h on 1024 cores for the turbulent cases. Each case was run with 1 GB of memory per core. The cores used were Intel Xeon E5-2698v3 (2.3 GHz). Ten simulations were conducted at a Reynolds number of $Re = 500$, which resulted in laminar flow. One simulation was conducted at a Reynolds number of $Re = 5000$, for which the flow was turbulent. For the laminar cases, we considered three different initial dense fluid distributions where the cross section of the initial shape was varied. These were the planar, circular, and rectangular cross sections, denoted by the letters *P*, *C*, and *R* in Table I, respectively. The planar cross section corresponds to a rectangular cross section whose lateral extent spans the entire width of the numerical domain, i.e., $L_y = l_y$. As for the turbulent simulation, only the rectangular cross section was considered. The aspect ratio for the rectangular shape was based on a scaled-down design of an actual barge that was used in the experiments of Wei Er *et al.* (2016). The dimensions for the circular (respectively, planar) shape were based on the rectangular shape, in that the diameter (respectively, width) was equal to the width of the rectangle l_x (see Fig. 1). The domain size was chosen large enough to accommodate unhindered development of the thermal in all three directions. The large domain size also ensured that the results are independent of the release orientation.

Spectral elements are not uniformly distributed within the domain. They are rather skewed toward the upper center portion of the domain, as shown in Fig. 2, as this is the region where the largest velocity and density gradients occur.

Boundary conditions for the velocity and density must be specified on all six boundaries. For the density field, a zero flux boundary

TABLE I. List of simulations. α is the vertical gap between the uppermost layer of the dense fluid and the upper boundary of the numerical domain (see Fig. 3), and $l_x \times l_y \times l_z$ denote the initial dimensions of the dense fluid. FS and NS denote the velocity condition applied at the top boundary as free-slip and no-slip, respectively. *n* is the polynomial order. *Re* and *Sc* are the Reynolds and Schmidt numbers. The domain size ($L_x \times L_y \times L_z$) and the grid resolution ($N_x \times N_y \times N_z$) are chosen to ensure a domain- and grid-independent solution. The letters *R*, *P*, and *C* in the simulation name refer to the cross-sectional shape of the initial dense fluid. They denote the rectangular, planar, and circular shapes, respectively.

Sim name	α	Upper BC	$L_x \times L_y \times L_z$	$l_x \times l_y \times l_z$	*n*	*Sc*	*Re*	$N_x \times N_y \times N_z$
*R*1	1.0	FS	36 × 36 × 30	0.5848 × 2.924 × 0.5848	8	1	500	24 × 24 × 32
*R*2	1.0	FS	36 × 36 × 30	0.5848 × 2.924 × 0.5848	24	1	5000	24 × 24 × 32
*C*1[a]	1.0	FS	36 × 36 × 36	0.5848 × 0.5848 × 0.5848	8	1	500	24 × 24 × 32
*P*1	1.0	FS	36 × 10.8 × 30	0.5848 × 10.8 × 0.5848	8	1	500	24 × 24 × 32
*P*2	0.5	FS	36 × 10.8 × 30	0.5848 × 10.8 × 0.5848	8	1	500	24 × 24 × 32
*P*3	0.2	FS	36 × 10.8 × 30	0.5848 × 10.8 × 0.5848	8	1	500	24 × 24 × 32
*P*4	0.0	FS	36 × 10.8 × 30	0.5848 × 10.8 × 0.5848	8	1	500	24 × 24 × 32
$P1_{NS}$	1.0	NS	36 × 10.8 × 30	0.5848 × 10.8 × 0.5848	8	1	500	24 × 24 × 32
$P2_{NS}$	0.5	NS	36 × 10.8 × 30	0.5848 × 10.8 × 0.5848	8	1	500	24 × 24 × 32
$P3_{NS}$	0.2	NS	36 × 10.8 × 30	0.5848 × 10.8 × 0.5848	8	1	500	24 × 24 × 32
$P4_{NS}$	0.0	NS	36 × 10.8 × 30	0.5848 × 10.8 × 0.5848	8	1	500	24 × 24 × 32

[a] l_x and l_y correspond to the diameter of the circular cross section for *C*1.

Published under license by AIP Publishing

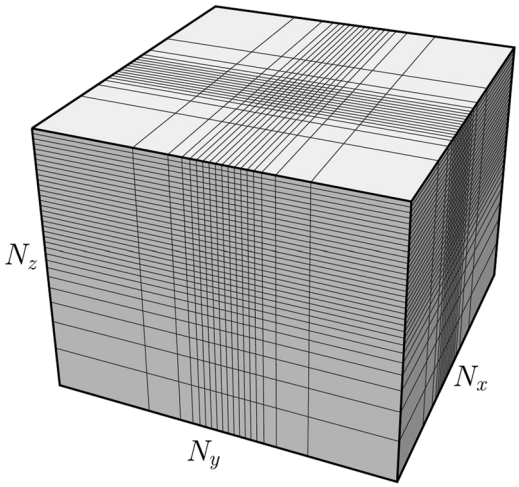

FIG. 2. Element distribution in the numerical domain. The elements are skewed toward the upper center portion of the domain for increased efficiency.

condition was specified on all domain boundaries, namely,

$$\nabla\rho \cdot \boldsymbol{e}_n = 0, \tag{9}$$

where $\boldsymbol{e}_n$ is the unit normal at each boundary. As for the velocity field, the free-slip condition was enforced at the top boundary, while a zero pressure outflow condition was enforced on the remaining five boundaries,

$$\begin{aligned} \nabla\boldsymbol{u} \cdot \boldsymbol{e}_n &= 0, \\ p &= 0. \end{aligned} \tag{10}$$

Regarding the initial condition, the velocity was set to zero in the entire domain for both the dense and ambient fluids. As for the density field, it was generated using error functions to make sure that the interface is of finite thickness. A finite thickness interface is required due to the spectral nature of the code, and it accounts for any mixing that occurs between the heavier fluid and the surrounding lighter fluid before the release. The heavy fluid was not always placed in direct contact with the upper boundary. There was a vertical gap of ambient fluid at the top, of height $\alpha = 1$, separating the heavy fluid from the upper domain boundary, as shown in Fig. 3.

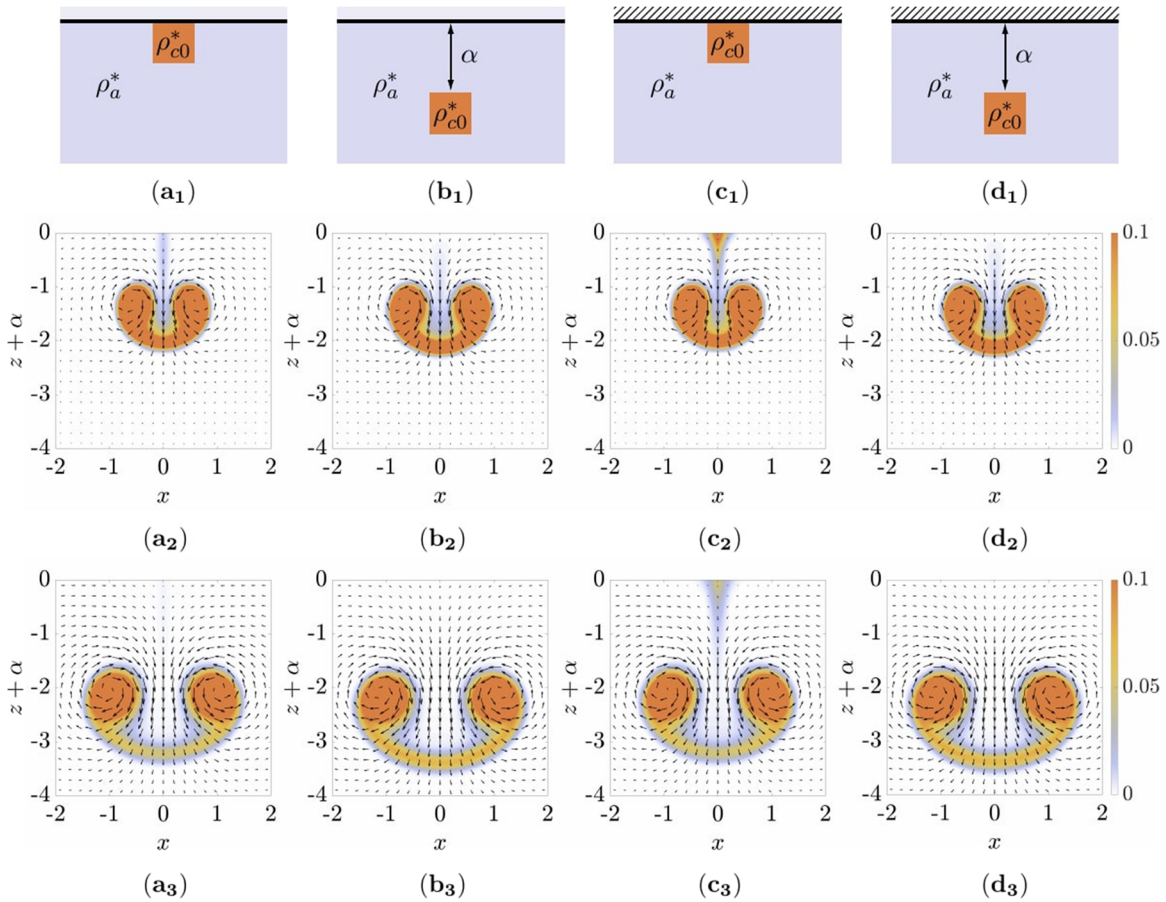

FIG. 3. Iso-contours of density overlain by the instantaneous velocity vectors in the $y = 0$ plane. The first row illustrates the initial condition, while the second and third rows correspond to snapshots at $t = 5$ and $t = 10$, respectively. Columns a, b, c, and d correspond to cases $P4$, $P1$, $P4_{NS}$, and $P1_{NS}$, respectively. The contour color bars are not representative of the instantaneous density range but are chosen for clarity as the maximum density of the thermal decreases with time.

Published under license by AIP Publishing

B. Influence of top boundary

The purpose of this section is to shed some light on how qualitatively and quantitatively the initial placement of the dense fluid and the enforced top boundary condition may affect the short-term and long-term evolution of the thermal. For this section, we consider the planar geometry. Starting from the basic settings shown in Table I, eight cases are tested by changing the vertical gap α = [0.0, 0.2, 0.5, 1.0] and the top boundary condition (free-slip vs no-slip). Here, the vertical gap α corresponds to the initial gap between the domain's upper surface and the uppermost layer of the dense fluid, as shown in Fig. 3. In the interest of brevity, only the two extreme cases with $\alpha = 0.0$ and $\alpha = 1.0$ are shown in Fig. 3.

Figure 3 shows the instantaneous velocity vector plot in the $y = 0$ symmetry plane along with iso-contours of concentration to discern the shape and location of the thermal. Snapshots are shown at the time of release ($t = 0$) and at two later time instances $t = 5$ and $t = 10$. The results indicate that both the vertical gap and the type of boundary condition (free-slip vs no-slip) on the upper wall affect the evolution of the current.

When the dense fluid is placed in direct contact ($\alpha = 0$ in Fig. 3) with the upper boundary, we observe the formation of a tail of dense fluid that extends all the way from the thermal to the top boundary. This tail forms shortly after release and persists until around $t = 10$, as shown in Fig. 3. The formation of the tail depends on the proximity of the release from the domain upper boundary. It is observed to be independent of the type of boundary condition (free-slip vs no-slip) that is applied. The tail is, however, thicker when the no-slip boundary condition is enforced. On the contrary, when the ambient fluid gap is large enough ($\alpha = 1$ in Fig. 3), the tail is practically non-existent. When the ambient fluid gap is very small, the upper centermost part of the dense fluid remains nearly stationary and experiences very little mixing. As such, it continues to feed dense fluid to the symmetry plane, which results in the formation of the tail. On the contrary, when the vertical gap is large enough, the entire dense fluid is set in motion, which explains the absence of a tail.

Additionally, we find the presence of a vertical gap to change the shape of the thermal. When the dense fluid is initially in contact with the upper boundary, we find the two vortex tubes that form to be closer to one another than in the case where an initial ambient fluid gap is present. Finally, we find the flow field to be visibly different in the cases considered in Fig. 3. When the gap is present, we observe a wider down flow region of ambient fluid that extends farther upward as compared with the zero vertical gap cases. This flow pattern is to be expected since the presence of an upper barrier and the thin layer of overlying ambient fluid will both act to hinder the downward component of flow as the thermal descends.

In addition to the aforementioned qualitative differences, we also find the presence of an ambient fluid gap to increase the downward propagation speed of the thermal. In Fig. 4(a), we plot the distance traveled by the front of the thermal along the z-axis, $z_F - z_{F0}$. Here, z_F and z_{F0} correspond to the instantaneous and initial positions of the front. We observe the sensitivity of downward speed of the thermal on the vertical gap α to become marginal for values near $\alpha = 1$. However, for smaller values of α, we observe the thermal to descend at slower speeds. For instance, by $t = 18$, we find the thermal with a sufficiently large initial gap $\alpha = 0.5$ to cover around

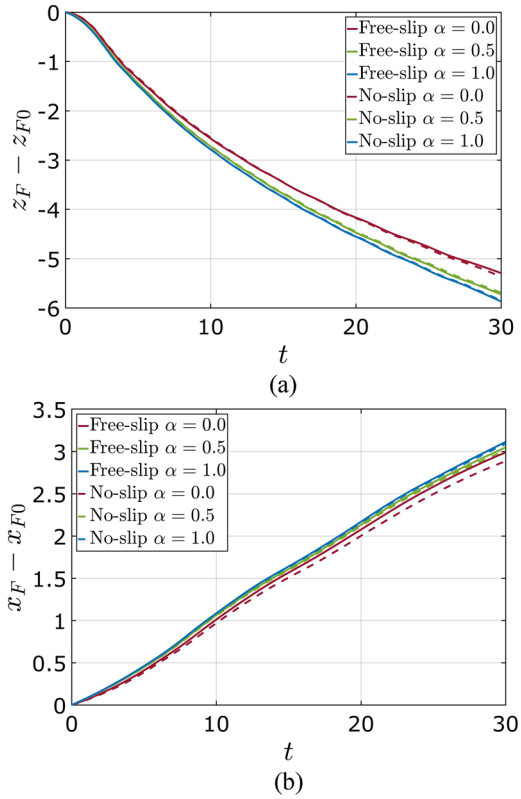

FIG. 4. Temporal evolution of (a) the traveled distance along the z-axis $z_F - z_{F0}$ and (b) temporal evolution of the horizontal spreading distance along the x-axis $x_F - x_{F0}$. In both panels, the front is defined by the threshold density value ρ_{th} = 0.001. α denotes the extent of the ambient fluid vertical gap (see Fig. 3).

8% more distance than a thermal initially in contact with the upper boundary ($\alpha = 0$). Similar conclusions can be drawn according to the horizontal spreading distance, as shown in Fig. 4(b). Here, similarly, x_F and x_{F0} correspond to the instantaneous and initial values of the outermost extent of the thermal along the x-axis, respectively. A comparison between panels (a) and (b) indicates that horizontal spreading is less sensitive to the vertical gap than vertical spreading. Figure 4(b) also shows that for $\alpha = 0$, there is a slightly larger difference in the horizontal spreading distance between the no-slip and free-slip cases when compared to the difference in vertical spreading in Fig. 4(a), where the free-slip case extends slightly farther in the horizontal direction. One possible explanation is that the horizontal outward spreading is partly due to the presence of the vortex tube. As the thermal descends, the rotation of the vortex tube generates a lift force that propels the thermal horizontally outward. A slight reduction in the rotational speed of the vortex due to the no-slip condition could result in a slight reduction in the horizontal lift force. This will in turn lead to the observed behavior in Fig. 4(b).

By using a very simple analysis, we can provide a crude estimate of the initial vertical gap that is needed between the upper surface of the numerical domain and the top layer of the thermal to minimize or eliminate the effect of the upper boundary condition. Note that the effects of the upper boundary are not to be avoided necessarily;

Published under license by AIP Publishing

here, we only aim to show that a vertical gap does modify the flow and its influence should be accounted for in similar studies.

In formulating an estimate of the gap, we consider the same canonical planar case. The initial shape of the dense fluid mimics that in the simulations with height $\tilde{H}$ and width $\tilde{W}$, placed at a distance α from the top wall. At the time of release, the dense fluid will advance downward with a characteristic velocity $\tilde{U}$. This characteristic velocity will act to displace ambient fluid immediately below the thermal, with a flow rate per unit width of approximately

$$\tilde{Q} = \tilde{U}\widetilde{W}. \tag{11}$$

In fact, because of continuity, the same fluid that is being displaced below the thermal must be "replenished" above the thermal. If the thermal is sufficiently removed from the top wall, the ambient fluid will reach the top surface of the thermal by intruding horizontally through the gap of height α. If we restrict the average velocity of the intruding fluid to $\tilde{U}$, then α may be straightforwardly obtained from continuity as

$$\alpha = \widetilde{W}/2. \tag{12}$$

We find the above value of α to be of the same order as that obtained with the DNS. From Fig. 4, we find the upper boundary effects to become negligible beyond $\alpha \cong 0.5$, which correspond to $\tilde{W}/1.2$ instead of $\tilde{W}/2$. As noted in Table I, $\tilde{W} = 0.5848$, and thus, $\tilde{W}/1.2 \approx 0.5$. In the present study, the initial placement of the dense fluid is sufficiently removed from the upper boundary ($\alpha = 1$) such that the latter does not play a role in modifying the dynamics of the thermal.

III. RESULTS

This section will primarily focus on the results from the laminar simulations, specifically the non-canonical rectangular case $R1$. As will be shown later on, the gross characteristics of the turbulent case $R2$ are largely similar to the laminar case.

First, we start by validating our simulations against the experiments of Sànchez *et al.* (1989). Their experiments consisted of releasing a spherical cup of brine solution 10 ml in volume into tap water. They performed several experiments at Reynolds numbers ranging between 520 and 1000. Our corresponding simulation, thus, consisted of releasing a sphere of relatively denser solution into a relatively less dense ambient. Consistent with the aforementioned scaling, the non-dimensional diameter of the spherical solution was $D_0 = 1.24$. To better mimic the experimental conditions, the sphere was put in contact with the upper boundary at which the free-slip condition was enforced. The simulation was conducted at $Re = 1000$. Remaining parameters were identical to those in simulation $C1$ in Table I.

We plot the largest diametral extent of the thermal against the distance traveled in Fig. 5. The data are normalized by the initial diameter of the release. Here, D represents the instantaneous largest diametral extent of the thermal, and $z_{D0}-z_D$ corresponds to the traveled distance measured at the location of the largest diametral extent. Note that z is positive upward and, thus, z_D is a negative quantity as the thermal descends upon release. The symbols in the figure correspond to the experimental results of Sànchez *et al.* (1989), where each color indicates a specific value of the Reynolds number in the aforementioned range of 520–1000. We find our simulation to correctly reproduce the same trend observed in the experiments. We should note here, however, that the reason we do not display the magnitudes for the Reynolds number for the various experiments in Fig. 5 is because Sànchez *et al.* (1989) made a point of not specifying the Reynolds number. In fact, this is done not just in this figure but in all figures of Sànchez *et al.* (1989). This would imply that the spread in the data is not primarily due to the Reynolds number but rather due to the variations from one realization to another. In this regard, we do not compare with an individual realization; rather, we look at the ensemble of all realizations. Here, we observe that the simulation falls well within the spread of the experimental data.

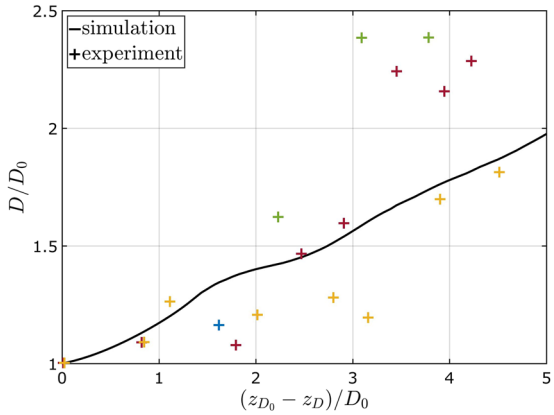

FIG. 5. Largest diametral extent vs distance traveled. The solid line corresponds to the present simulation, and symbols correspond to the experiments of Sànchez *et al.* (1989), with each color representing a specific value of the Reynolds number ranging between 520 and 1000.

A. Flow structure

In this section, we elaborate on the three-dimensional flow structure of the thermal and explain some interesting characteristics pertaining to the rectangular cross section and other non-canonical thermals in general. In Fig. 6, panels (a), we show semi-transparent iso-surfaces of density at six equally spaced time instances between $t = 0$ and $t = 25$, whereas in panels (c) and (d), we show iso-contours of density within the y-z and x-z symmetry planes, respectively. Additionally, in panels (a), (c), and (d), the thermal is visualized within a fixed portion of the domain to track its growth and position over time with respect to the initial release. In panel (b), a blown-up view is considered. Here, three semi-transparent iso-surfaces provide information on the density distribution within the thermal. The three iso-surface values are $\rho = 0.1$, 0.01, and 0.001. The colors associated with each are red, green, and blue, respectively. While in the axially symmetric case, the current forms a circular vortex ring (e.g., Turner, 1969), here the rectangular initial shape leads shortly after release to the formation of an elliptical-like vortex tube (see $t = 5$ and $t = 10$). Only at later times does the vortex ring take on a circular shape, however, with azimuthally varying strength. The largest density within the thermal still resides at the center of the tube, as indicated by the red iso-surface in the (b) panels.

Published under license by AIP Publishing

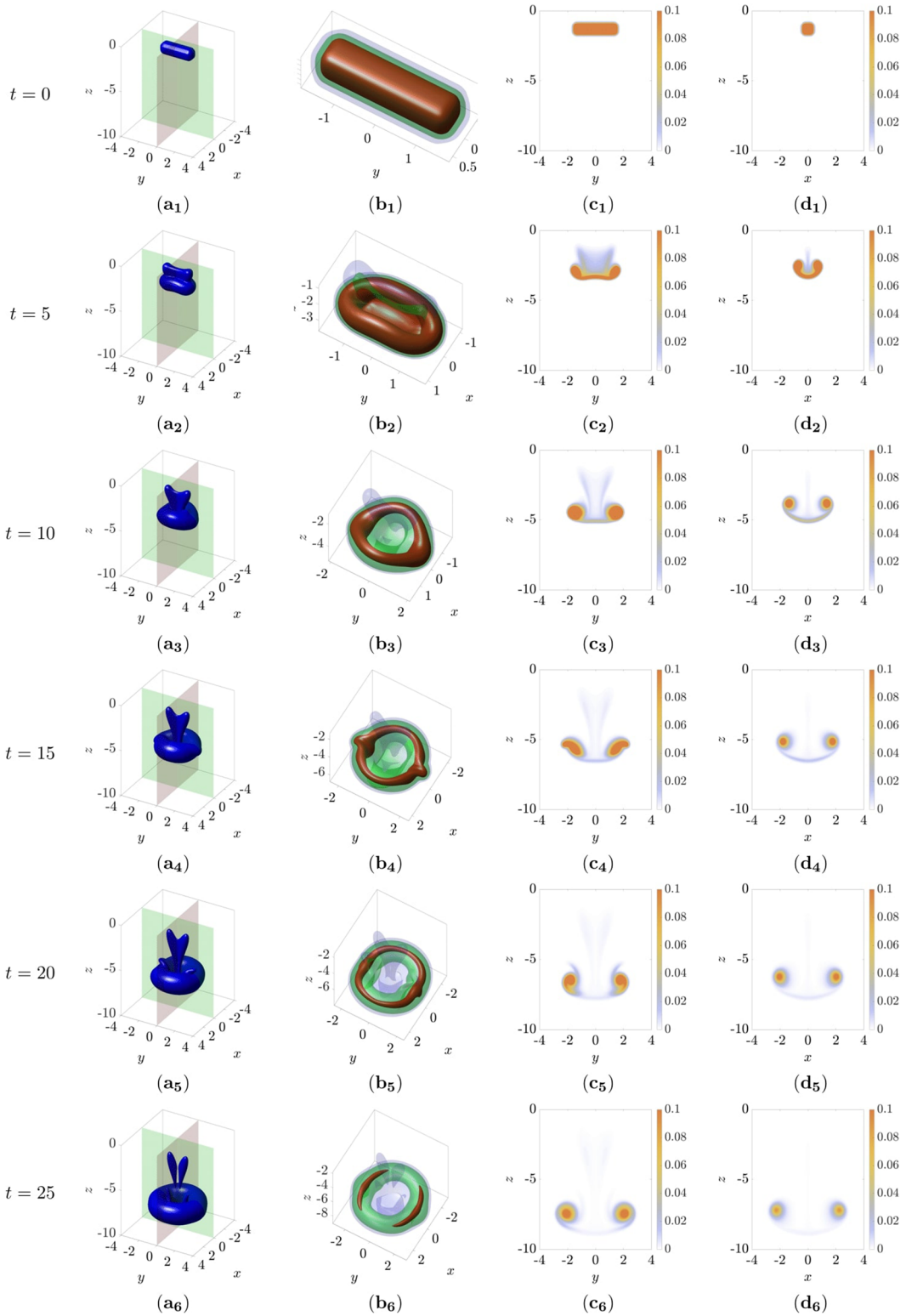

FIG. 6. Results from R1 for the (a) iso-surfaces of ρ = 0.001. (b) Enlarged view through three semi-transparent iso-surfaces of density ρ = 0.001 (blue), ρ = 0.01 (green), and ρ = 0.1 (red). (c) Density iso-contours in the x = 0 and (d) y = 0 symmetry planes.

Published under license by AIP Publishing

While in the laminar circular case, the vortex tube maintains axial symmetry during descent with no azimuthal variation, this is not observed for the rectangular case. The vortex tube does preserve its four-way symmetry but exhibits strong azimuthal variations in elevation. It is readily visible in the (b) panels, especially at $t = 5$ and $t = 10$, that the thermal is elevated along its short edge within the $y = 0$ symmetry plane but plunges downward progressively as it approaches the tips of its long edge within the $x = 0$ symmetry plane. At $t = 5$, we find the vertical location of the points of highest density in panels (c_2) and (d_2) to be approximately −2.9 and −2.5, respectively, which results in about a 14% relative difference in elevation between these two locations. Consequently, by $t = 10$, the vertical locations become −4.5 (panel c_3) and −3.8 (panel d_3), and the relative difference grows to reach approximately 15%.

Additionally, it is also clear from Fig. 6 that the thermal does not expand horizontally outward at the same rates along its initial short and long edges, the x and y axes, respectively. We find the average rate of expansion along the x-axis from the start of the simulation until $t = 10$ to be over two folds that along the y-axis. Another interesting aspect is the non-uniform thickness of the vortex tube, specifically the variation in thickness along the azimuthal direction. It is also evident from Fig. 6 that beyond $t = 5$, the tube is noticeably thicker along the initial long edge compared to the short edge. Finally, we note that beyond $t = 10$, the vast majority of the dense fluid resides in the vortex tube.

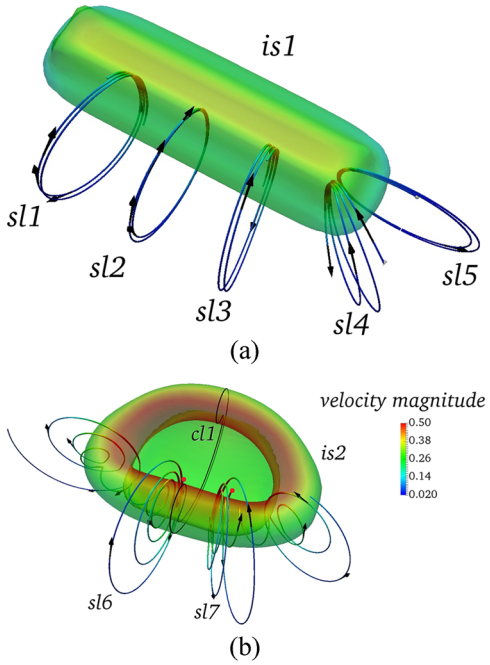

FIG. 7. (a) Density iso-surface colored by velocity magnitude at $t = 1$. The current is visualized with streamlines sl1 through sl5 and semi-transparent iso-surface is1 of density $\rho = 0.1$. (b) Same as panel (a) for $t = 5$. The two red dots mark the starting points for streamlines sl6 and sl7. The current is visualized with streamlines sl6 and sl7 and semi-transparent iso-surface is2 of density $\rho = 0.1$. The iso-surface intersects with the x-z-center slice at centerline cl1. The two velocity contours share the same color map.

B. A helical path within the vortex tube

The azimuthal variation in the thermal resulting from the non-canonical nature of the release produces some interesting dynamics, which may be visualized from the streamlines at close proximity to or within the thermal. In Fig. 7, we show the thermal at two time instances in panels (a) and (b) at $t = 1$ and $t = 5$, respectively. A semi-transparent iso-surface of density $\rho = 0.1$ shows the three-dimensional structure of the thermal. The iso-surfaces are colored using the velocity magnitude, and the color map displayed in panel (b) applies for panel (a) as well.

At $t = 1$, the thermal still closely resembles its initial shape and forms an elongated cylinder oriented along the y-axis. The vortex tube is yet to develop but is clearly in the process of forming as the velocity magnitude at the core of the thermal is larger than at the extremities. We show five streamlines predominantly in one quadrant of the thermal. Due to the laminar nature of the flow, streamlines at other locations in the thermal may be inferred from symmetry. In fact, only four streamlines are unique (sl2 through sl5), while streamline sl1 is a mirror image of sl3.

The streamlines take on the shape of circular loops passing through both the thermal and the ambient fluid. In the portion occupied by the ambient fluid, the streamlines reflect the upward direction of the flow, while within the thermal, the flow direction is downward. Additionally, the velocity magnitude is not uniform along the streamline, being larger in the downward direction. This is evident from the color map and is to be expected as the negatively buoyant thermal propagates downward.

Streamlines sl2 and sl5 remain confined to the x-z and y-z symmetry planes, respectively. This is again an implication of the symmetrical and laminar nature of the flow. A fluid parcel in either the x-z or y-z plane has no tendency to propagate azimuthally or linearly in either direction and, thus, remains confined to the vertical plane in which it originated. However, as we deviate away from the symmetry planes, and because of the non-canonical nature of the release, we observe an azimuthal component of the flow. This is apparent from the spring-like shape that the streamline presumes. For example, in the case of sl3, we find that the streamline has expanded along the y-direction, indicating a y-component of the flow. Additionally, we find streamlines in regions of strong curvature variation (in the shape of the thermal) to span out more visibly than other regions. This is apparent in sl4, for which the separation between the loops of the streamline is the largest for that time instant.

At $t = 5$, the streamlines have become more complex. Here, again we use the $\rho = 0.1$ iso-contour to illustrate the structure of the thermal. We show only two streamlines, sl6 and sl7. sl6 originates just to the left of the x-z symmetry plane denoted by cl1 in Fig. 7, while sl7 originates slightly farther away and on the other side of the x-z plane. The iso-contour is again colored by velocity magnitude and exhibits faster speeds on the interior of the vortex tube where the velocity points downward, in the same direction the thermal travels. What is interesting in the image is the appearance of a helical motion that initiates close to the x-z plane and weaves its way within the vortex tube toward the y-z plane.

By inspecting streamline sl6, we find that it initiates relatively far from the axis of the vortex tube and makes its way toward the

Published under license by AIP Publishing

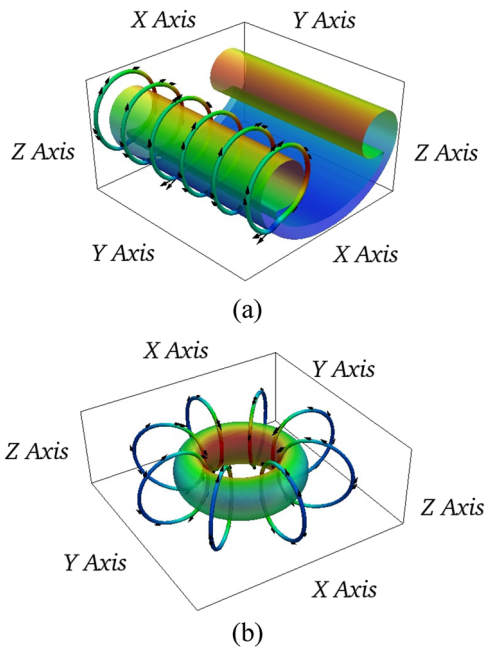

FIG. 8. Snapshot of the current at $t = 5$ for the (a) planar and (b) axially symmetric cases from simulations $P1$ and $C1$, respectively. The current is visualized with streamlines and a semi-transparent density iso-surface of $\rho = 0.1$. The iso-surface is colored by the local velocity magnitude. Since the current is rotating and descending, the magnitude of velocity is larger in the descending (inner) portion of the vortex tube.

latter in a circular motion. The streamlines do not form co-centric circles with respect to the axis of the vortex tube. We find the stream paths to be more (respectively, less) closely spaced toward the interior (respectively, exterior) of the tube. Additionally, every time the streamline completes a full revolution around the tube, its velocity increases, as apparent from the color scheme. We also note that before the streamline becomes completely immersed inside the iso-contour $\rho = 0.1$, it remains primarily in the same vertical plane from which it originated, deviating only slightly in the y-direction. The helical motion of the streamline begins once the latter is completely engulfed inside the $\rho = 0.1$ iso-contour, i.e., in the region of relatively elevated density. The streamline continues its helical motion and only begins to spiral outward as it approaches the y-z plane, with the velocity magnitude decreasing every time the streamline wraps around the vortex tube.

In contrast to the streamlines from the non-canonical rectangular case ($R1$), we observe, as expected, no azimuthal component of velocity in either the canonical planar ($P1$) or axially symmetric ($C1$) cases in Fig. 8, panels (a) and (b), respectively. Here, we show the current at only one time instance $t = 5$. We use the same semi-transparent iso-surface $\rho = 0.1$ to locate the thermal. Similar to Fig. 7, the iso-surface is colored by velocity magnitude.

While the direction of the flow in the helical streamline inside the vortex tube is directed from the x-z plane toward the y-z plane, the outside portion of the streamline is directed in the opposite direction. This is to be expected as there should be no mean cross-flow component. Nonetheless, there could be a non-zero mean flow for the dense fluid, provided of course there is an equivalent return flow of ambient fluid in the opposite direction. This non-zero mean flow of dense fluid is the subject of Sec. III C.

C. A non-zero mean cross-flow component

The helical streamline motion discussed in Sec. III B showed a migration of dense fluid from the initial short edge of the rectangle (x-z plane) to the initial long edge (y-z plane). This helical migration is a consequence of the non-canonical nature of the release. To demonstrate that such a migration is not only present at a specific time instance but rather occurs over a finite time span, we plot in Fig. 9 the vector field with components $\hat{m}_x$ and $\hat{m}_y$ corresponding to the density-weighted, vertically integrated horizontal components of velocity u and v,

$$\begin{cases} \hat{m}_x(x,y,t) = \int_0^{L_z} \rho(x,y,z,t)u(x,y,z,t)dz, \\ \hat{m}_y(x,y,t) = \int_0^{L_z} \rho(x,y,z,t)\mathrm{v}(x,y,z,t)dz. \end{cases} \tag{13}$$

The integrated density and vector fields from Eqs. (13) and (14) are shown in Fig. 9 at three time instances, namely, $t = 1$, 5, and 10. Shortly after release at $t = 1$, the vector field components $\hat{m}_x$ and $\hat{m}_y$ are nearly zero within the interior of the thermal. At this early time, the flow in the interior of the thermal is pointing mainly vertically downward. Since $\hat{m}_x$ and $\hat{m}_y$ do not account for this vertical component of velocity, they will attain near zero values. On the other hand, near the outer edge of the thermal, the vector field is predominantly aligned normally outward. We observe, however, a slight tilting inward in the vector field toward the $y = 0$ symmetry

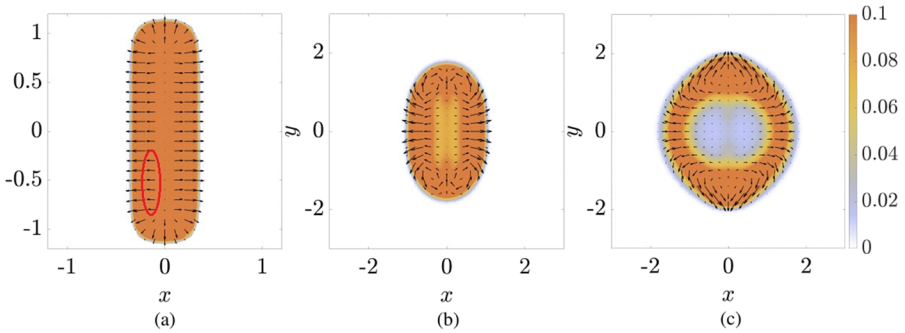

FIG. 9. Iso-contours of the vertically integrated density field overlain by vectors corresponding to the density-weighted, vertically integrated horizontal components of velocity. Panels (a), (b), and (c) correspond to $t = 1$,5, and 10, respectively. The red ellipse in panel (a) points to the converging flow toward the $y = 0$ symmetry plane.

Published under license by AIP Publishing

plane. This tilting is non-existent near the short edge of the thermal but is evident farther away, which is in accord with the direction of flow observed from the streamlines in Fig. 7 at the same time instant $t = 1$. This converging flow is very similar to that observed in non-canonical finite-release gravity currents on horizontal (Zgheib *et al.*, 2017) and inclined (Zgheib *et al.*, 2016 and Zhu *et al.*, 2017) surfaces shortly after release.

To help orient the integrated vector field with respect to the thermal, the latter is represented by iso-contours of the vertically integrated density field, $\hat{\rho}_z$,

$$\hat{\rho}_z(x,y,t) = \int_0^{L_z} \rho(x,y,z,t)dz. \tag{14}$$

By $t = 5$, we observe flow reversal where the $\hat{m}_y$ component clearly points away from the $y = 0$ symmetry plane. This diverging flow has never been observed before, at least in the context of thermals. In fact, for non-canonical, initially rectangular, gravity currents, a converging cross-flow component has previously been reported by Zgheib *et al.* (2017), that is, the cross-flow occurred in the opposite direction to that presently observed. Even though both thermals and gravity currents are solely driven by buoyancy, it is peculiar that they display a cross-flow velocity component in opposite direction to one another. We note the increased outward normal component of the flow along the $y = 0$ plane in comparison with that along the $x = 0$ plane. The persistence over time of this difference in velocity leads to the change in the cross section of the thermal from being initially rectangular at time of release to nearly circular by $t = 10$.

Finally at $t = 10$, we continue to observe the higher accumulation of dense fluid around the vortex core and its strong migration toward the initial major axis of the thermal. Due to this continued dense fluid migration, there is now a strong disparity in dense fluid accumulation between the initial major and minor axes of the thermal.

D. Swirling strength

Another aspect of the flow which will be useful in providing possible explanations for the aforementioned effects of the non-canonical nature of the thermal is the swirling strength λ_{ci}. The swirling strength provides a good metric for identifying regions of intense vortical structures (Zhou *et al.*, 1999 and Chakraborty *et al.*, 2005). It is mathematically defined as the absolute value of the imaginary portion of the complex eigenvalue of the velocity gradient tensor. In this section, we will focus on the swirling strength within the symmetry x-z and y-z planes. In Fig. 10, we show iso-contours of λ_{ci} in the aforementioned planes at $t = 5$. The purpose of this figure is to illustrate the difference in swirling strength between the two symmetry planes. The vortex in the x-z plane is visibly stronger. This difference is a direct result of the rectangular shape of the initial release.

At the start of the simulation, there is no discernible azimuthal variation in the thermal; however, once the rectangular vortex tube develops, we begin to observe the effects of the non-canonical shape discussed in Secs. III A and III C. In fact, as the vortex tube rotates about its axis, it does not only move the dense fluid around, but it must as well carry and displace with it a portion of the ambient

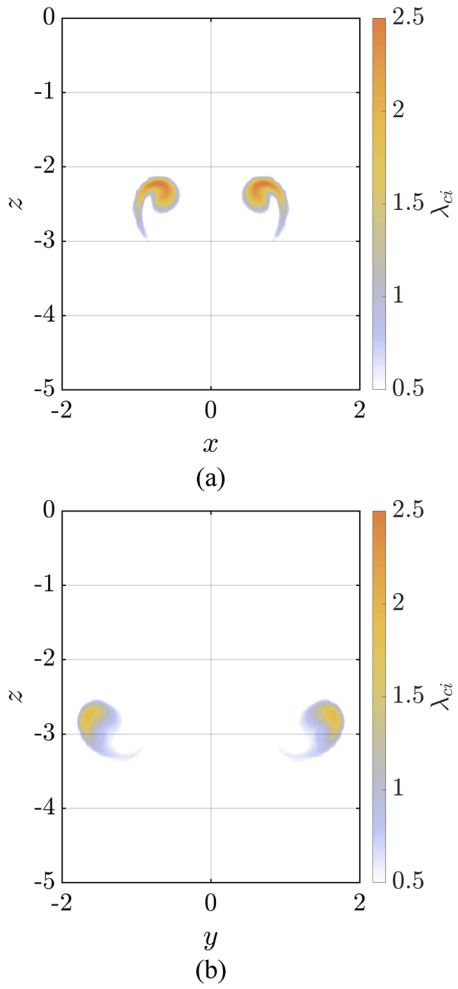

FIG. 10. Iso-contours of the swirling strength λ_{ci} in the x-z and y-z symmetry planes at $t = 5$.

fluid in contact with the vortex tube. In the straight portion of the thermal (which originally corresponds to the long edge of the rectangle), the length of the vortex tube remains unchanged as it sinks downward and propagates horizontally outward. Therefore, the volume of ambient fluid that is being displaced by the vortex tube does not change significantly with time, assuming that this volume is linearly proportional to the length of the tube. On the other hand, the curved portion of the vortex tube's length increases with time as the latter spreads horizontally outward. It follows that the amount of ambient fluid that is being displaced and rotated by the vortex tube increases with time as well.

IV. DISCUSSION

The non-canonical nature of the release leads to interesting dynamics that are not present in the canonical axially symmetric or planar cases. These dynamics are a result of the initial azimuthal variation due to the initially non-axisymmetric shape of the dense

Published under license by AIP Publishing

fluid. These variations were observed in multiple aspects including the thickness of the vortex tube, the disparity in the vertical and horizontal velocity components, as well as the dense fluid migration (i.e., the cross-flow component). A possible explanation for each of these dynamics will be given below.

A. Disparity in the horizontal velocity component

As the negatively buoyant vortex tube plunges downward, its rotation about the tube axis generates a lift force in the normal direction to its downward path. The stronger the vortex, the stronger the lift force and the faster the horizontal component of the velocity. Because the strength of the vortex is not uniform along the azimuthal direction, the lift force and, consequently, the horizontal component of velocity will vary around the vortex tube. As seen in Fig. 10 and discussed in Sec. III D, the vortex is strongest along the *x*-*z* symmetry plane and weakest along the *y*-*z* symmetry plane with smooth azimuthal variation between these two locations (not shown in the figure). It, therefore, follows that the horizontal outward normal component of velocity will be largest along the *x*-*z* plane and progressively decreases to its minimum value as it approaches the *y*-*z* plane. Additionally, because the disparity in vortex strength persists for a prolonged period of time, the initially rectangular thermal will tend toward a more circular-like shape over time.

Figure 11 shows the horizontal distance traveled by the thermal as well as the corresponding velocity along the *x* (red solid line) and *y* (red dashed line) axes from *R*1. These curves are contrasted by the corresponding values from *P*1 (blue) and *C*1 (green). For the rectangular case *R*1, the thermal clearly travels faster along the *x*-axis than it does along the *y*-axis. However, what is more interesting is that the horizontal speed along the *x*-axis is even larger than that of the canonical planar case *P*1. A possible explanation for this occurrence is that contrary to the planar case, the elliptical (or rectangular) vortex tube is constantly being stretched as the thermal descends. The stretching of a vortex tube is known to increase its intensity (Lacaze *et al.*, 2010 and Albagnac *et al.*, 2011). It follows that a stronger vortex tube will lead to a stronger lift force and, consequently, to even faster speeds along the *x*-axis. Needless to say, in the case of a spanwise-invariant planar case, there is no vortex stretching.

It should be noted here that the aforementioned non-uniform horizontal spreading is not unique to non-canonical thermals. It has been observed in gravity currents (e.g., Zgheib *et al.*, 2015a; 2015b) and jets (e.g., Quinn, 1989 and Gutmark and Grinstein, 1999). However, the mechanism for each of the three cases is different. In the case of gravity currents, the non-uniform spreading is a result of the initial partitioning of the dense fluid in the very early stages of the release (Zgheib *et al.*, 2015a; 2015b). In the case of jets, and elliptic jets in particular, the non-uniform horizontal/cross-flow spreading is a result of differing shear layer growth rates. The shear layer along the flattest side of the jet grows relatively faster, which leads to larger entrainment rates and, consequently, a faster horizontal/cross-flow spreading rate (Quinn, 1989 and Gutmark and Grinstein, 1999).

B. Disparity in the vertical velocity component

Even though the rectangular release was perfectly horizontal at the start of the simulation, the vortex tube, shortly after its development, becomes concave downward along the *y*-*z* plane (see Fig. 6).

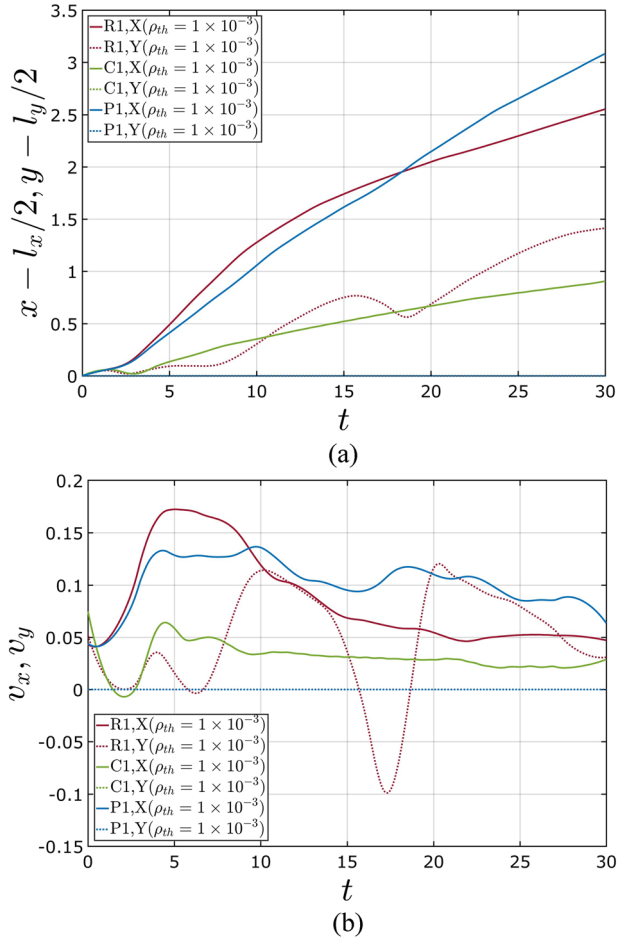

FIG. 11. Horizontal distance traveled along the *x* and *y* axes from *R*1 (red), *P*1 (blue), and *C*1 (green).

That is the vortex tube is at a higher elevation in the *x*-*z* plane than in the *y*-*z* plane. This indicates that in addition to the aforementioned azimuthal variation in horizontal speed of the thermal, there is clearly an azimuthal variation in the downward speed as well. One possible explanation for this behavior is as follows. Since the vortex tube admits a horizontal component of velocity, its path is not strictly vertical but rather inclined at some angle θ with respect to the vertical *z*-axis. This angle is not uniform along the azimuthal direction. It is largest in the *x*-*z* plane and smallest in the *y*-*z* plane, where the horizontal speed is largest and smallest, respectively. Since the lift force generated from the rotation of the vortex tube is normal to the path of the tube, it follows that this lift force will not be purely horizontal but will rather have an upward *z*-component. The magnitude of this component is proportional to the sine of the inclination angle θ. Since θ is largest (respectively, smallest) in the *x*-*z* (respectively, *y*-*z*) plane, then the z-component of the lift force will be largest (respectively, smallest) along that plane as well. To add to the previous effect, not only is the vertical component of the lift force largest in the *x*-*z* plane, but also the strength of the vortex tube

Published under license by AIP Publishing

is largest in the x-z plane as well. Both of these effects lead to the vertical disparity in the vertical velocity component.

There is also another aspect likely responsible for the disparity in the thermal vertical speed. By comparing the temporal evolution of the front position from the canonical cases $P1$ and $C1$ in Fig. 12, it is clear that the thermal from the circular case advances the fastest downward. This faster downward propagation is likely due to the induced flow generated from the rotation of the vortex tube. Indeed, as the vortex tube rotates, it not only puts the dense fluid in rotation but also induces a rotation of the surrounding ambient fluid. The induced rotation of ambient fluid has its downward component above the dense fluid and will, thus, act to speed the descent of the thermal. Because of its axisymmetric nature, the induced flow is stronger in the circular than in the planar case. To put the above discussion in the context of the non-canonical rectangular release, it follows that the circular portion in the rectangular release will be subject to a stronger induced flow than the initially straight portion of the release. This is in agreement with the aforementioned disparity in vertical speed along the x-z and y-z planes.

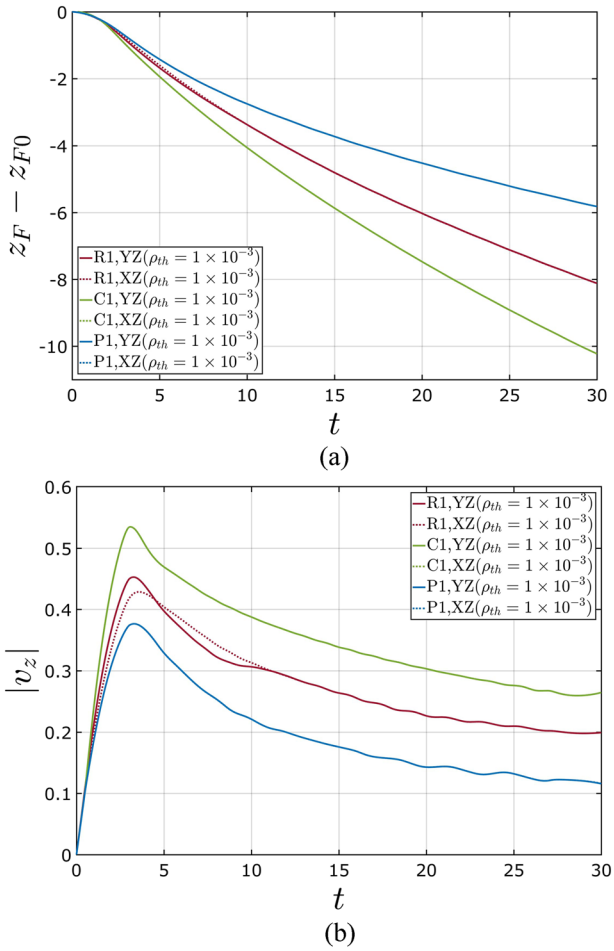

FIG. 12. (a) Temporal evolution of the vertical front position from $R1$ (red), $P1$ (blue), and $C1$ (green). (b) Absolute value of the z-component of velocity for the front of the thermal.

C. Dense fluid helical migration

A cross-stream dense fluid migration has been previously reported in the context of non-canonical gravity currents (Zgheib *et al.*, 2016; 2017). While both thermals and gravity currents are driven solely by buoyancy, they do not share the same mechanism behind the cross-flow component. In the context of gravity currents, the cross-flow migration of the dense fluid occurred in the opposite direction (away from the initial short edge of the rectangle) to that observed presently and was primarily attributed to a difference in dynamic pressure within the head of the gravity current (Zgheib *et al.*, 2016).

From Fig. 9, we find that the dense fluid, shortly after release (t = 1), in fact admits a small but finite cross-flow component toward the x-z plane. It is only after the vortex tube forms at t = 2 that we begin to observe a net dense fluid migration away from the x-z plane. A possible reason for this migration is the vertical height disparity in the vortex tube between the x-z and y-z planes, the latter being lower than the former. As the thermal sinks faster along the y-z plane, it sucks in nearby dense fluid. This is consistent with the fact that as the vertical disparity between these two locations increases with time, so does the magnitude of the diverging cross-flow component.

As for the helical nature of the flow, it arises from two factors. The first is the rotating flow in a vertical plane normal to the vortex tube, and the second is the aforementioned cross-flow component. The superposition of both these flow components results in the helical motion observed in Fig. 7.

D. Effects of higher *Re*

All results shown thus far correspond to the laminar simulations in Table I. However, we will show in this section that the disparity of horizontal and vertical speeds as well as the cross-flow migration of dense fluid may be equally applicable, if not amplified, in turbulent flows. We consider simulation $R2$, the non-canonical thermal with an initially rectangular cross section. Details of which are listed in Table I.

In Fig. 13, we use semi-transparent iso-surfaces of density to show a close-up view of the thermal from the turbulent simulation $R2$ at t = 10. We observe, as stated earlier, the same dynamics as for the laminar simulation $R1$. We should note here that we have additionally considered two values of the Reynolds number, namely, Re = 300 in the laminar regime and Re = 3000 in the turbulent regime, and we did not observe any qualitative differences with respect to the results shown above. From the nearly circular shape at the time instant considered in Fig. 13, it is clear that the thermal advances faster along the x-z symmetry plane than it does along the y-z symmetry plane. Furthermore, it is obvious that the vortex tube shown in red is not at the same horizontal level but takes on a shape similar to the laminar counterpart. The tube is elevated along the x-z symmetry plane but dips downward along the y-z symmetry plane. Furthermore, it is clear from the figure that there is accumulation of dense fluid along the tips of the initial major axis similar to what was observed in the laminar case (Fig. 6). In fact, we find the accumulation of heavy fluid to be visibly larger in the turbulent case than it is in the laminar case. The accumulation of heavy fluid along the tips of the initial major axis of release is again due to a dense fluid migration similar to that observed in Fig. 9. It should be noted here,

Published under license by AIP Publishing

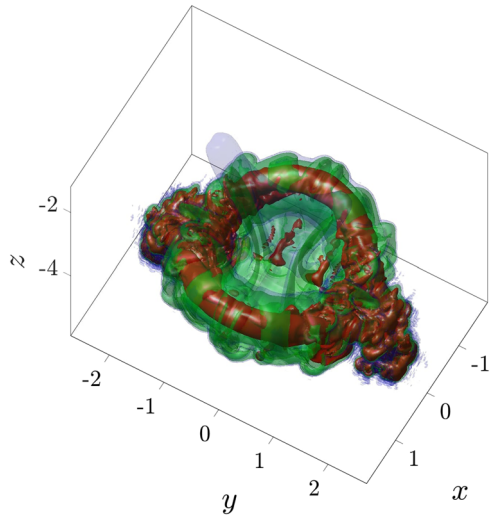

FIG. 13. Semi-transparent iso-surfaces of density from *R*2 at t = 10. The red, green, and blue colors correspond to density iso-values of 10^{-1}, 10^{-2}, and 10^{-3}, respectively.

however, that the turbulent results are preliminary and require more extensive investigation.

Additionally, we compare the temporal evolution of the thermal front location from the turbulent *R*2 case to the experiments of Wei Er *et al.* (2016). In their experiment, Wei Er *et al.* (2016) released a dense solution with an identical shape to that used in the present simulation. The released volume in the experiments was, however, larger than that in the present simulation which resulted in a larger Reynolds number of around 25 000. The results of the comparison are shown in Fig. 14. Here, z_F is the instantaneous location of the thermal front and z_{F0} is the initial location of the thermal front. The difference $z_F - z_{F0}$, thus, represents the traveled distance of the thermal. We find that the simulation consistently

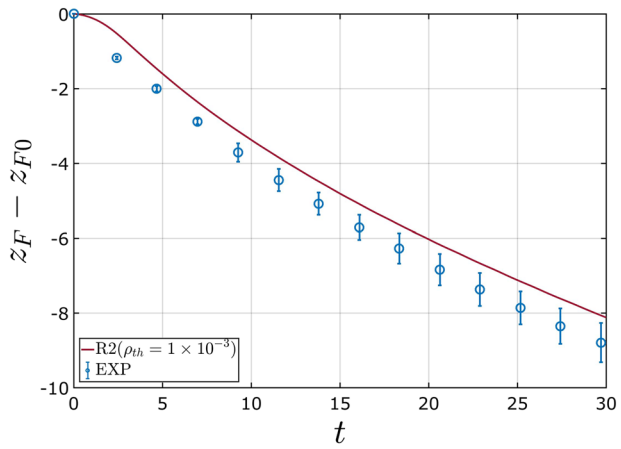

FIG. 14. Vertically traveled distance vs time. The solid line corresponds to the present simulation. The experiment pertains to Wei Er *et al.* (2016).

underestimates the front position but exactly replicates the trend of the experimental data. In fact, such behavior where turbulent simulations correctly capture the behavior of corresponding experiments at higher Reynolds numbers has been previously reported in other types of buoyancy driven flows such as gravity currents (e.g., Blanchette *et al.*, 2005 and Cantero *et al.*, 2007). This indicates Reynolds number independence once a turbulent state is reached, at least for the quantities that are being investigated. The underestimation of the front position, however, may be due primarily to the difference in the release mechanism between the simulation and the experiment. The release of the dense fluid in the simulation is ideal in the sense that there is no perturbation to the surrounding fluid at the time of release. On the other hand, the release of the dense fluid in the experiments significantly perturbs both the dense and ambient fluids. The release is achieved by opening a pair of symmetric rectangular half shells, which are connected by a horizontal hinge on their top edge. The container shell rotation inevitably induces local fluid vortices, which may affect the evolution of the thermal.

V. CONCLUSIONS

We presented results from direct numerical simulations on the evolution of negatively buoyant thermals under laminar and turbulent flow conditions. Three different initial density profiles were studied. These included the canonical planar and axially symmetric cases as well as the non-canonical rectangular case. We first showed that the release location of the dense fluid with respect to the upper surface does influence the downward speed and structure of the thermal. More specifically, when the dense fluid is initially at close proximity from the upper surface, a tail of dense fluid forms and persists for a significant period of time. No tail, however, forms when the release is sufficiently removed from the upper surface. Additionally, the dense fluid released at close proximity to the upper boundary advances more slowly than the same dense fluid released sufficiently far from the upper boundary.

By plotting the three-dimensional streamlines for the non-canonical rectangular case, we demonstrate the presence of a cross-flow component that is otherwise not present in the canonical cases. This cross-flow component is shown to follow a helical path and to result in a net dense fluid migration away from the initial short edge of the rectangular release. The direction of cross-flow was in the opposite sense to that reported in gravity currents with the same initial density distribution. While both thermals and gravity currents are solely driven by buoyancy, the mechanisms leading to the cross-flow are different in each flow.

In the case of rectangular thermals, the cross-flow was shown to be a result of azimuthal variations in induced flow and vortex tube strengths. The induced flow was stronger near the far edges in the rectangular case, while the vortex tube was stronger near the short edge. Both aspects were shown to result in faster downward propagation near the far edge of the thermal, which in turn leads to a cross-flow of dense fluid away from the initial short edge.

Finally, while the majority of the analysis was conducted for laminar flows, we showed that the dynamics corresponding to the non-canonical nature of the release are also present and may be even amplified at higher Reynolds numbers. It should be noted, however, that the turbulent results are preliminary and require more extensive investigation.

Published under license by AIP Publishing

ACKNOWLEDGMENTS

We are grateful to ExxonMobil Upstream Research Company for providing support through Grant No. EM09296.

REFERENCES

Albagnac, J., Lacaze, L., Brancher, P., and Eiff, O., "On the existence and evolution of a spanwise vortex in laminar shallow water dipoles," Phys. Fluids **23**(8), 086601 (2011).

Blanchette, F., Strauss, M., Meiburg, E., Kneller, B., and Glinsky, M. E., "High-resolution numerical simulations of resuspending gravity currents: Conditions for self-sustainment," J. Geophys. Res.: Oceans **110**(C12), 1978–2012, https://doi.org/10.1029/2005jc002927 (2005).

Bond, D. and Johari, H., "Effects of initial geometry on the development of thermals," Exp. Fluids **39**(3), 591–601 (2005).

Bonometti, T. and Balachandar, S., "Effect of Schmidt number on the structure and propagation of density currents," Theor. Comput. Fluid Dyn. **22**, 341–361 (2008).

Cantero, M. I., Lee, J. R., Balachandar, S., and Garcia, M. H., "On the front velocity of gravity currents," J. Fluid Mech. **586**, 1–39 (2007).

Chakraborty, P., Balachandar, S., and Adrian, R. J., "On the relationships between local vortex identification schemes," J. Fluid Mech. **535**, 189–214 (2005).

Fischer, P. F., Lottes, J. W., and Kerkemeier, S. G., nek5000 web page, http://nek5000.mcs.anl.gov, 2008.

Gao, L. and Yu, S. C. M., "Vortex ring formation in starting forced plumes with negative and positive buoyancy," Phys. Fluids **28**(11), 113601 (2016).

Gutmark, E. J. and Grinstein, F. F., "Flow control with noncircular jets," Annu. Rev. Fluid Mech. **31**, 239–272 (1999).

Hasnain, A. and Alba, K., "Buoyant displacement flow of immiscible fluids in inclined ducts: A theoretical approach," Phys. Fluids **29**(5), 052102 (2017).

Huppert, H. E. and Simpson, J. E., "The slumping of gravity currents," J. Fluid Mech. **99**(4), 785–799 (1980).

Lacaze, L., Brancher, P., Eiff, O., and Labat, L., "Experimental characterization of the 3D dynamics of a laminar shallow vortex dipole," Exp. Fluids **48**(2), 225–231 (2010).

Lecoanet, D. and Jeevanjee, N., "Entrainment in resolved, turbulent dry thermals," arXiv:1804.09326 (2018).

Ottolenghi, L., Adduce, C., Inghilesi, R., Roman, F., and Armenio, V., "Mixing in lock-release gravity currents propagating up a slope," Phys. Fluids **28**(5), 056604 (2016).

Quinn, W. R., "On mixing in an elliptic turbulent free jet," Phys. Fluids A **1**, 1716–1722 (1989).

Richards, J. M., "Experiments on the penetration of an interface by buoyant thermals," J. Fluid Mech. **11**(3), 369–384 (1961).

Sànchez, O., Raymond, D. J., Libersky, L., and Petschek, A. G., "The development of thermals from rest," J. Atmos. Sci. **46**(14), 2280–2292 (1989).

Turner, J. S., "The motion of buoyant elements in turbulent surroundings," J. Fluid Mech. **16**(1), 1–16 (1963).

Turner, J. S., "The flow into an expanding spherical vortex," J. Fluid Mech. **18**(2), 195–208 (1964).

Turner, J. S., "Buoyant plumes and thermals," Annu. Rev. Fluid Mech. **1**(1), 29–44 (1969).

Wei Er, J., *et al.*, "Open-water disposal of barged sediments," J. Waterw. Port Coastal Ocean Eng. **142**(5), 04016006 (2016).

Zgheib, N., Bonometti, T., and Balachandar, S., "Dynamics of non-circular finite-release gravity currents," J. Fluid Mech. **783**, 344–378 (2015a).

Zgheib, N., Bonometti, T., and Balachandar, S., "Propagation and deposition of non-circular finite release particle-laden currents," Phys. Fluids **27**(8), 086604 (2015b).

Zgheib, N., Bonometti, T., and Balachandar, S., "Suspension-driven gravity surges on horizontal surfaces: Effect of the initial shape," Comput. Fluids **158**, 84–95 (2017).

Zgheib, N., Ooi, A., and Balachandar, S., "Front dynamics and entrainment of finite circular gravity currents on an unbounded uniform slope," J. Fluid Mech. **801**, 322–352 (2016).

Zhao, B., Law, A. W. K., Lai, A. C., and Adams, E. E., "On the internal vorticity and density structures of miscible thermals," J. Fluid Mech. **722**, R5 (2013).

Zhou, J., Adrian, R., Balachandar, S., and Kendall, T., "Mechanics for generating coherent packets of hairpin vortices," J. Fluid Mech. **387**, 353–396 (1999).

Zhu, S. J., Zgheib, N., Balachandar, S., and Ooi, A., "Front dynamics of elliptical gravity currents on a uniform slope," Phys. Rev. Fluids **2**(6), 064801 (2017).

Published under license by AIP Publishing